Journal of Hazardous Materials 459 (2023) 132122

Contents lists available at ScienceDirect

Journal of Hazardous Materials

journal homepage: www.elsevier.com/locate/jhazmat

Competitive photoelectrochemical aptamer sensor based on a Z-scheme Fe_2O_3/g-C_3N_4 heterojunction for sensitive detection of lead ions

Jingui Chen [a], Jinxiu Zhao [a], Rui Feng [a], Hongmin Ma [a], Huan Wang [a], Xiang Ren [a,*], Qin Wei [a,c], Huangxian Ju [b]

[a] Key Laboratory of Chemical Sensing & Analysis in Universities of Shandong, School of Chemistry and Chemical Engineering, University of Jinan, Jinan 250022, China
[b] State Key Laboratory of Analytical Chemistry for Life Science, College of Chemistry and Chemical Engineering, Nanjing University, Nanjing 210023, China
[c] Department of Chemistry, Sungkyunkwan University, Suwon 16419, Republic of Korea

HIGHLIGHTS

- Z-scheme Fe_2O_3/g-C_3N_4 serve as sensing matrix exhibited excellent PEC behavior.
- Z-scheme heterojunctioncan inhibit the recombination of e^-/h^+.
- ZnO is used as an aptamer label, which greatly reduces the detection limit.
- PEC sensor exhibited a low detection limit of 7.9 pg/mL for Pb^{2+}.

GRAPHICAL ABSTRACT

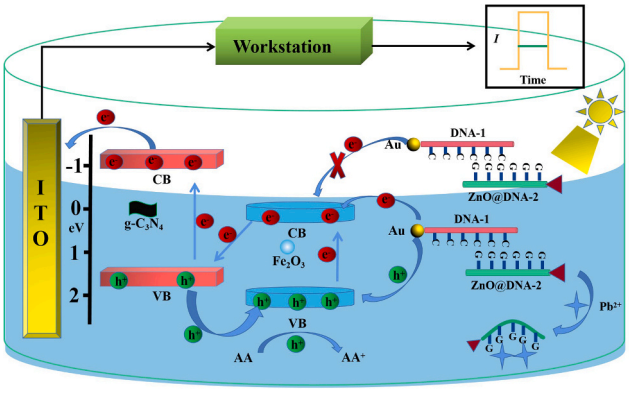

ARTICLE INFO

Editor: Lingxin Chen

Keywords:
Photoelectrochemical
Fe_2O_3/g-C_3N_4
ZnO
Lead ion

ABSTRACT

Lead ion (Pb^{2+}) is one of the heavy metal contaminants within the environment, which can seriously affect biological health. Thus, it is very important to detect lead ions, especially exceeding the standard concentration (100 ng/mL). In this work, we have developed a photoelectrochemical (PEC) aptamer sensor with Z-scheme Fe_2O_3/g-C_3N_4 heterojunction as a substrate material for sensitive detection of Pb^{2+}. Specifically, Fe_2O_3/g-C_3N_4 is employed as a substrate with a powerful and stable photocurrent response. Au and DNA-1 connected to the substrate material via the Au-S bond and increased the electron conduction. Marking DNA-2 with ZnO effectively reduced the light absorption intensity resulting in a lower photocurrent response. Surprisingly, the Pb^{2+} PEC sensor showed good linearity in the detection range of 62 pg/mL to 1 μg/mL with a detection limit as low as 7.9 pg/mL (S/N = 3). The sensor showed stable recovery and low relative standard deviation in real sample detection. Additionally, the sensor exhibited excellent stability, selectivity, and reproducibility. The reproducibility of the electrodes was evaluated, and the accuracy of the individual electrode current values was calculated to range from 0.5% to 2.71% with an RSD of 1.74%. Such PEC sensor guarantees to supply a brand-new approach to the detection of Pb^{2+}.

* Corresponding author.
E-mail address: chem_renx@163.com (X. Ren).

https://doi.org/10.1016/j.jhazmat.2023.132122
Received 18 May 2023; Received in revised form 14 July 2023; Accepted 20 July 2023
Available online 22 July 2023

1. Introduction

The difficulty of degrading heavy metals leads to their gradual accumulation in plants and animals that trickle down to humans at the top of the food chain, causing irreversible damage to them [1,2]. In the past time, people have targeted principally the way to treat the diseases caused by heavy metal ions but neglected the way to forestall heavy metal pollution [3,4]. The necessity for preventing serious metal pollution is to check for excessive heavy metal ions [5]. Therefore, a fast, sensitive, and correct detection mechanism ought to be established to deal with the period observation of serious metal ion concentrations within the surroundings.

There are many methods for detecting heavy metal ions, including electrochemical methods [6], atomic fluorescence photometry [7], differential pulse voltammetry [8], etc. However, these methods have the shortcomings of cumbersome operation steps, sophisticated instruments, long detection time, and low sensitivity. In recent years, photoelectrochemical (PEC) sensors have been applied to the detection of assorted environmental pollutants and illness markers owing to their easy detection, straightforward miniaturization, and high sensitivity [8,9]. The principle of PEC sensor is a device that uses photoelectric signal conversion to achieve the analysis of the concentration of the substance to be measured [10–14]. The advantages of PEC combined with the specificity of aptamers allow the design of PEC aptamer sensors with high sensitivity and high selectivity [15,16]. The development of photosensitive materials with efficient photoelectric conversion and the design of reasonable photoelectric detection methods are research focused on constructing high-performance PEC aptamer sensors.

Fe_2O_3 is widely used in photocatalysis as a result of its abundance, ease of preparation, and low cost [17]. The band gap of Fe_2O_3 is between 1.8 and 2.2 eV, leading to the skimpy light absorption capability and low photoelectrical conversion potency [18]. Single semiconductor materials are limited in PEC sensor fabrication due to insufficient light absorption capacity and slow electron transfer efficiency [19,20]. To improve these deficiencies with the following methods, the formation of heterojunctions between photosensitive materials can enhance the photocurrent response, and the metal element-sensitized semiconductors can improve the electron transport efficiency [21]. g-C_3N_4 could be a stratified nanoflake with an irregular arrangement made from C and N atoms covalently warranted along. The high chemical and thermal stability of g-C_3N_4 is imparted by the superposition of van der Waals force interactions power-assisted by layer-to-layer interactions [22]. g-C_3N_4 has a band gap width of about 2.7 eV and good absorption in visible light, which may combine with Fe_2O_3 to form a Z-scheme heterojunction structure that can accelerate the separation of electrons (e^-) and holes (h^+) [23]. Due to the accumulation of holes in the valence band of Fe_2O_3 and the accumulation of electrons in the conduction band of g-C_3N_4, strong oxidizing properties and reducing properties are maintained in a composite material.

In this way, Fe_2O_3/g-C_3N_4 maintains a stable photocurrent output. Additionally, Au nanoparticles immobilized DNA-1 can sensitize the substrate material and enhance electron transport efficiency [24]. ZnO, with a wide band gap of 3.4 eV, can only absorb ultraviolet light and is often used as a light absorption inhibitor to inhibit the light absorption ability of photosensitive materials [25]. ZnO limits the absorption of visible light, and DNA-2 increases steric hindrance. Therefore, marking DNA-2 with ZnO plays a synergistic role in reducing the photocurrent response. In this study, a competitive signal amplification PEC aptamer sensor is designed with Z-scheme Fe_2O_3/g-C_3N_4 heterojunction nanocomposites as a sensing platform and ZnO as a DNA-2 marker to detect Pb^{2+} (Scheme 1). Specifically, Fe_2O_3/g-C_3N_4 heterojunction has a stable photocurrent response. Au nanoparticles sensitized substrate material further enhances photocurrent response, and ZnO as a DNA-2 marker reduces the light absorption capability of the sensor. Complexes of lead ions and base G (Pb^{2+}-G4) chains are formed and detached from the electrode surface and dispersed in solution when Pb^{2+} is recognized by ZnO@DNA-2. As a result, the photocurrent response of the sensor becomes larger due to the increased visible light absorption capacity of the electrode and a decrease in steric hindrance. Accordingly, a signal-amplifying sensor was successfully constructed for the sensitive detection of Pb^{2+}. The sensor can be used to detect Pb^{2+} in general rivers and lakes and provides a new method for detecting heavy metal ions.

2. Experimental part

2.1. Reagents and apparatus are reported in Supplementary material

2.1.1. Preparation of Fe_2O_3/g-C_3N_4 composites

The synthesis of α-Fe_2O_3 and g-C_3N_4 are reported in supplementary materials. The experimental conditions are reported in Fig. S1. Fe_2O_3/g-C_3N_4 composites were prepared by the electrostatic self-assembly method. First, 1 g of g-C_3N_4 nanosheets were taken, and the pH was

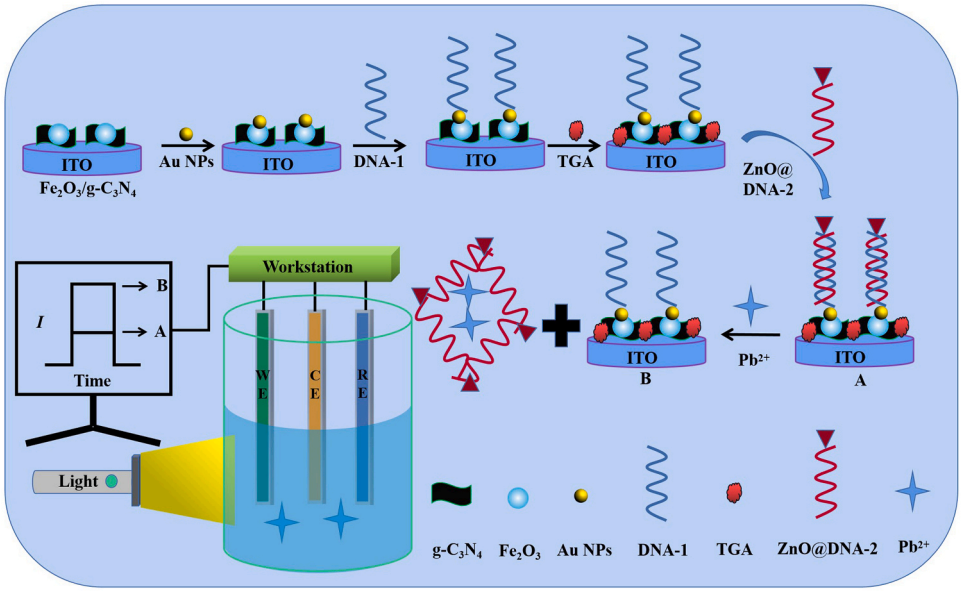

Scheme 1. Construction diagram of competitive PEC sensor.

adjusted to 6 by adding H_2SO_4 (0.2 M) solution dropwise. Then, 0.1 g of Fe_2O_3 powder was added to the above suspension under the condition of ultrasonication for 0.5 h. The homogeneous suspension was obtained after stirring for 4 h. Then, the solvent was removed by rotary evaporation. The synthesized mixed powder was washed several times with deionized water and methanol and then dried overnight in an oven at 80 °C.

2.1.2. Preparation of Au NPs

The Au NPs were prepared by reduction of sodium citrate. 1 mL of $HAuCl_4$ with a mass fraction of 2% was diluted in 200 mL of water. Then 5 mL of sodium citrate solution (1%) was added, with boiling for 15 min under vigorous stirring. The resulting solution was cooled and stored in a refrigerator at 4 ℃.

2.1.3. Construction of PEC sensor

The construction diagram of the PEC sensor is shown in Scheme 1. First, 30 μL (5 mg/mL) of Fe_2O_3/g-C_3N_4 composite was added dropwise on the surface of ITO (0.8 cm × 2.5 cm). After drying at room temperature, 10 μL of Au NPs solution was added dropwise and dried at 70 ℃ to obtain ITO/Fe_2O_3/g-C_3N_4/Au electrode. Further, 20 μL of 1.0 μM aptamer DNA-1 was incubated for 2 h at room temperature, and the sulfhydryl group of DNA-1 formed an Au-S bond with Au to self-assemble on the electrode. Then 20 μL of 0.1 mM thioglycolic acid (TGA) was added dropwise and incubated at room temperature to shield the non-specific sites. Finally, 20 μL of ZnO@DNA-2 was incubated for 2 h. The sensor construction was completed after natural air drying.

2.1.4. PEC measurement

Before testing, the constructed PEC sensor was fixed on the working electrode. In the three-electrode system, phosphate-buffered saline (PBS) with pH 6.8 was used as the buffer solution, and a self-assembled PEC workstation was used for the test. The photoelectric detection was performed using the i-t curve test as the output signal, and the light source was LED (The photocurrent was measured with a three-electrode system using a 300 W xenon lamp as light source, and the light source and the electrode was about 15 cm). The bias voltage is set to zero.

3. Results and discussion

3.1. Characterization of ZnO, Fe_2O_3, g-C_3N_4, and Fe_2O_3/g-C_3N_4

Fe_2O_3, g-C_3N_4, Fe_2O_3/g-C_3N_4, and ZnO were analyzed by X-ray diffractometer (XRD). In Fig. 1 A, it can be seen that the diffraction peaks of the synthesized Fe_2O_3 match perfectly with the position Fe_2O_3 standard card (JCPDS No. 33–0664), which proves that the Fe_2O_3 is successfully synthesized. The position of the strongest diffraction peaks of g-C_3N_4 is around 27°. We tested the XRD of the Fe_2O_3/g-C_3N_4 composite and interestingly found that the diffraction peaks matched well with Fe_2O_3 and g-C_3N_4, indicating the successful synthesis of the composite. Fig. 1B shows the XRD pattern of ZnO, from which it can be seen that the individual crystallographic planes of ZnO can correspond exactly to the standard card (JCPDS No. 36–1451). In addition, no other spurious peaks were found in the spectra, which proves the successful synthesis of ZnO.

Scanning electron microscopy (SEM) was used for the morphological analysis of Fe_2O_3, g-C_3N_4, and Fe_2O_3/g-C_3N_4. Fig. S2A shows the scanning electron microscope image of the bare ITO surface. As shown in Fig. 2A, Fe_2O_3 is presented as spherical, uniformly distributed nanospheres with sizes ranging from 45 to 55 nm. As shown in Fig. 2B, g-C_3N_4 shows irregular nanosheet-like structures clustered together. Fig. 2 C shows high-resolution transmission electron microscopy images of g-C_3N_4 at different scales. In Fig. 2D and Fig. S2B, it can be seen that Fe_2O_3 reacts with g-C_3N_4 and forms a heterogeneous structure by electrostatic adsorption uniformly distributed on the surface of g-C_3N_4. Fig. 2E shows high-resolution transmission electron microscopy images of Au NPs, spheroids with uniform distribution, and a diameter of about 10 nm. Fig. 2 F shows a ZnO scanning electron microscopy image that is uniformly distributed and has a diameter of around 30 nm — 40 nm. As shown in Fig. S2C, there is a film-like substance on the surface after the modification of DNA-1 and ZnO@DNA-2. After modification by lead ions, the membrane-like material was reduced (Fig. S2D), proving the shedding of ZnO@DNA-2. The elemental mapping image is shown in Fig. S3, and the elements of C, N, Fe, and O all exist in the image and are evenly distributed.

X-ray photoelectron spectroscopy (XPS) was used to study the element surface atomic composition and chemical valence states of Fe_2O_3/g-C_3N_4. As shown in Fig. 3 A, the elements C, N, Fe, and O are present in the full XPS spectrum of Fe_2O_3/g-C_3N_4 [22]. Fig. 3B shows the XPS high-resolution spectra of the C 1 s of g-C_3N_4 at 282.3 eV and 286.5 eV diffraction peaks, corresponding to the surface indeterminate carbon and sp^2 hybridized carbon in the (N = C—N) aromatic ring, respectively. In Fig. 3 C, the charge effects at 396.1 eV, 397.3 eV, 398.2 eV, and 402.2 eV diffraction peaks belong to the sp^2 hybrid nitrogen on the triazine ring, the tertiary nitrogen on the carbon bond, the amino nitrogen, and the charge effects in the heterocycle, respectively. Furthermore, as shown in Fig. 3D, the diffraction peaks of the lattice oxygen and surface hydroxyl groups of the O 1 s of Fe_2O_3 are at 529.8 eV and 530.6 eV. In the Fe XPS pattern (Fig. 3E), two distinct diffraction peaks appear at approximately 708.2 eV and 722.6 eV, corresponding to Fe $2p_{3/2}$ and Fe $2p_{1/2}$, respectively. Interestingly, the electron binding energy of each element is shifted, which is the composite heterostructure construction. The binding energy of lattice oxygen in Fe_2O_3 in the composite is smaller than that of pure Fe_2O_3 due to the transfer of

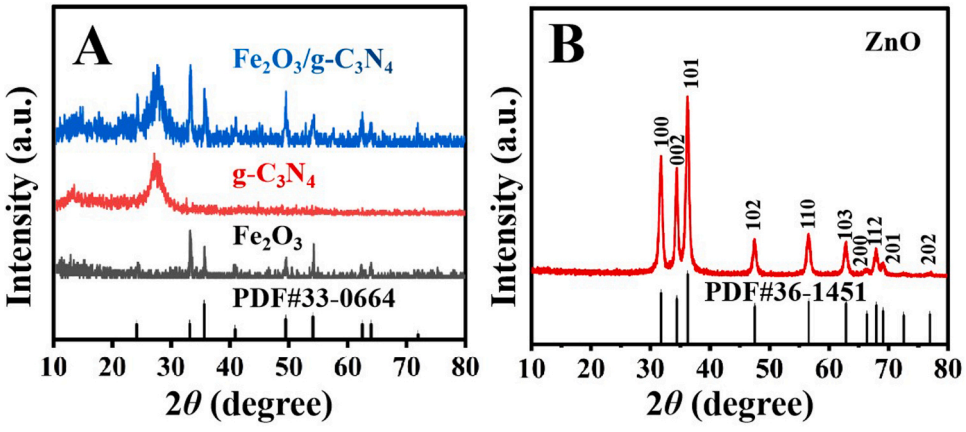

Fig. 1. (A) XRD patterns of Fe_2O_3, g-C_3N_4, and Fe_2O_3/g-C_3N_4. (B) XRD patterns of ZnO.

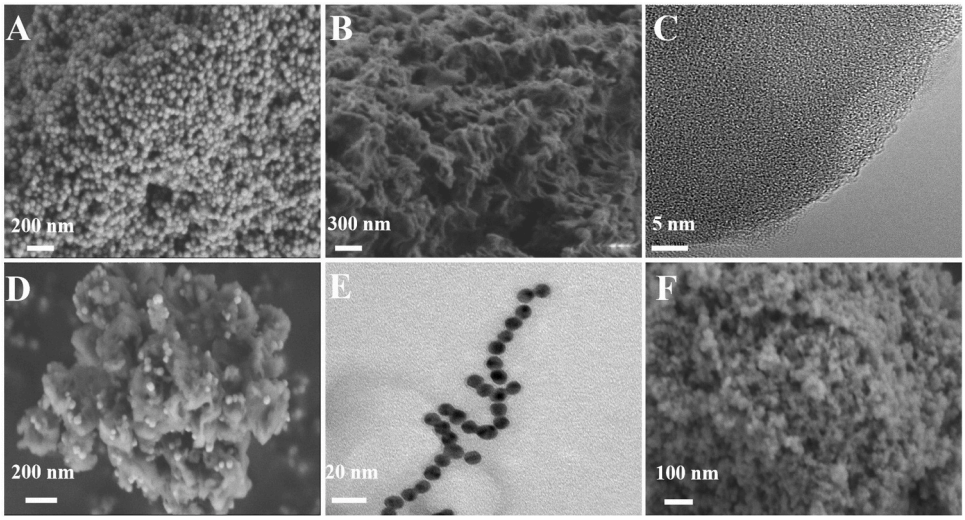

Fig. 2. (A) SEM of Fe_2O_3, (B) SEM of g-C_3N_4, (C) TEM of g-C_3N_4, (D) SEM of Fe_2O_3/g-C_3N_4, (E) TEM of Au NPs, (F) SEM of ZnO.

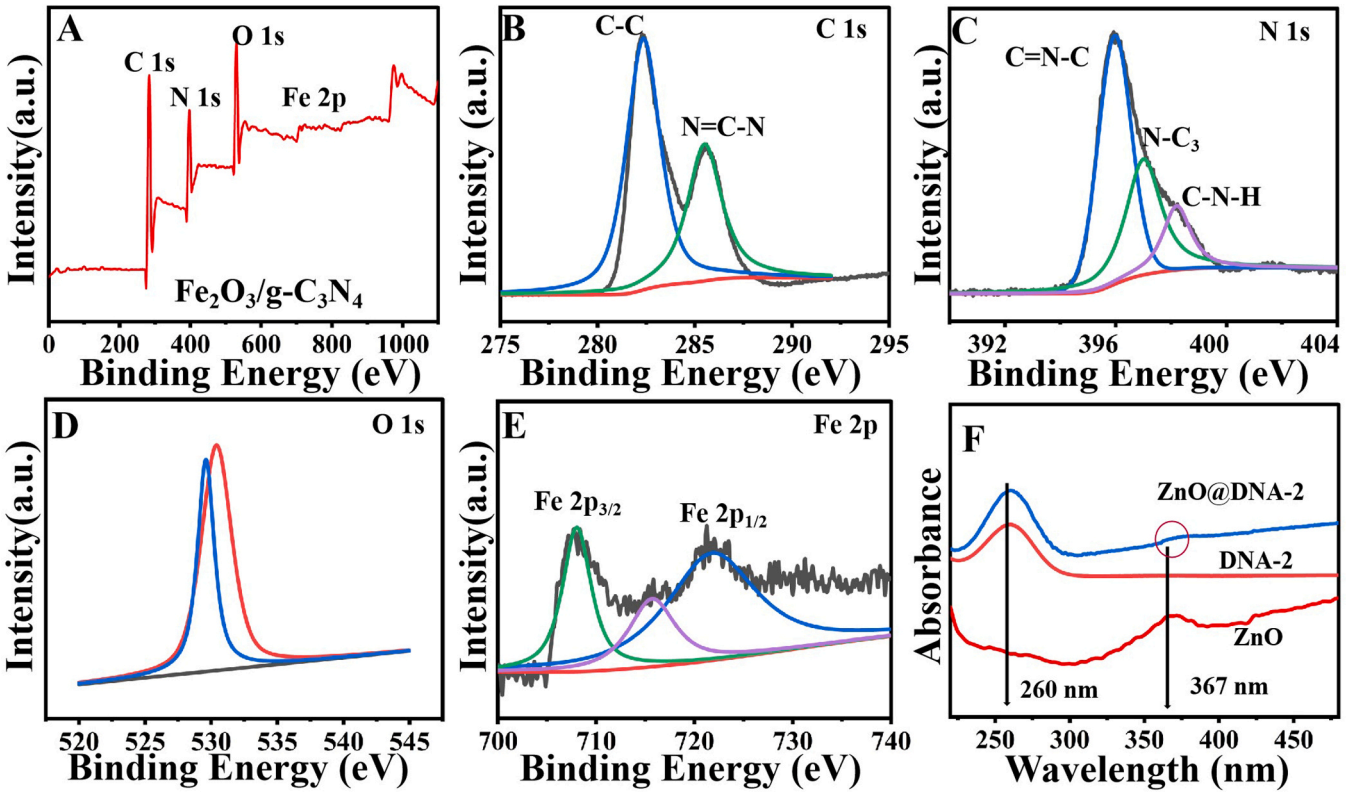

Fig. 3. (A) XPS survey spectrum of Fe_2O_3/g-C_3N_4 composite; high-resolution X-ray photoelectron spectrum for (B) C 1 s, (C) N 1 s, (D) O 1 s, (E) Fe 2p; (F) UV absorption spectra of ZnO, DNA-2, and ZnO@DNA-2.

electrons from Fe_2O_3 to g-C_3N_4. The above results indicate that the composite Fe_2O_3/g-C_3N_4 is not a simple physical adsorption interaction, but a strong interaction is formed. These interactions lead to the formation of heterostructures that enhance the electron transport capacity, thus increasing the photocurrent response of the substrate material. Fig. S4 shows the telescopic vibration of N-H has two-pointed absorption bands at 3438 and 3338 cm^{-1}. The bending vibration of N-H is absorbed in 1604 cm^{-1}. The antisymmetric telescopic vibration of Si-O-Si is at 1062 cm^{-1}. The absorption position of the Si-C bond is 1010 cm^{-1}. The above information indicates the success of the amination of ZnO, which can be linked to the carboxyl group of DNA-2 to form an amide bond.

Fig. 3 F shows the UV absorption spectra of ZnO, DNA-2, and ZnO@DNA-2. At the 367 nm position, ZnO has an absorption peak, which is its characteristic absorption peak. At around 260 nm, base G has a characteristic absorption peak. The absorption peak of ZnO@DNA-2 is present at both 260 nm and 367 nm. The above results indicate that ZnO and DNA-2 are successfully ligated by amide bonds.

3.2. Comparison of PEC signal

To improve the photocurrent response of the substrate material Fe_2O_3, several improvements were to the substrate material. Fig. 4 A

shows our comparison of the photocurrent response of Fe_2O_3, which is weak at 0.5 μA (curve a). Therefore, the Z-scheme heterojunction structure formed by g-C_3N_4 and Fe_2O_3 enhances electron transport and increases the photocurrent response to 2.0 μA (curve d). The addition of Au increases the photocurrent response of the electrode to 2.5 μA (curve g) due to its superconductivity. The formation of Au-S covalent bonds between DNA-1 and Au increases the spatial site resistance, which increases the impedance and decreases the photocurrent response to 2.2 μA (curve f). Due to the addition of the TGA, the current drops slightly to 2.1 μA (curve e). DNA-1 and DNA-2 are linked by complementary base pairing, which further increases the spatial site resistance due to the amide bond formed by joining the amino group on ZnO and the carboxyl group of DNA-2, further reducing the photocurrent response to 0.6 μA (curve b). When lead ions are present, they compete with DNA-1 for DNA-2 to generate G (Pb^{2+}-G4) chain bodies, which are subsequently dispersed in the solution. At this time, the potential spatial resistance becomes smaller, and the photocurrent response increases to 1.6 μA (curve c). The explanation of the effect of surface plasmon resonance of Au NPs on the photocurrent is seen in Fig. S5. This also proves our expected experimental results and provides a theoretical basis for the construction of a signal amplification sensor.

3.3. Comparison of the rating current impedance of the sensor

Electrochemical impedance spectroscopy (EIS) experiments are common means of characterization during sensor construction. To demonstrate the success of the material modification, impedance experiments were performed for the layer modification of the sensor. Specifically, the open-circuit voltage is 0.18 V, the amplitude of the alternating current is 5 mV, and the frequency is from 0.1 to 100000 Hz. The test solution containing 0.1 mol/L KCl and 2.5 mmol/L $[Fe(CN)_6]^{4-/3-}$. Fig. 4B, a built-in figure, shows the Randles equivalent circuit diagram, including electron transfer resistance (R_{et}), solution resistance (R_s), bilayer capacitance (C_{dl}), and diffusion impedance (Z_w). In addition, ZSimpWin software was used to fit the EIS data, and the specific values were obtained, as shown in Table S1. Curve a (36.23 Ω) shows the R_{et} curve of the substrate material ITO/Fe_2O_3. Curve b (62.52 Ω) shows the R_{et} curve of the substrate material ITO/Fe_2O_3/g-C_3N_4. Au NPs were dropwise coated on the substrate material, and the impedance value was further increased (curve c, 118.12 Ω), indicating that the gold nanoparticles were successfully modified. The steric hindrance of the electrode increases after incubation with DNA-1 (curve d, 143.58 Ω). Due to the addition of TGA, the impedance increases to 155.7 Ω (curve e). When ZnO@DNA-2 goes to capture DNA-1, the electron transfer ability of the sensor becomes weaker due to the synergistic effect of ZnO and DNA-2 to increase the spatial site resistance, and the impedance value increases substantially at this time (curve g, 364.32 Ω). G (Pb^{2+}-G4) chains are formed and detached from the electrode surface and dispersed in solution when Pb^{2+} in solution is recognized by ZnO@DNA-2. As a result, the photocurrent response of the sensor becomes larger due to the increased visible light absorption capacity of the electrode and decrease in steric hindrance (curve f, 263.45 Ω). The EIS experimental results of the sensor and the PEC response coincide, which proves the successful preparation of the sensor.

3.4. Electron transfer mechanism

A diagram of the possible electron transfer mechanism for the detection of Pb^{2+} by the competitive PEC sensor is shown in Fig. 5. As shown in Fig. S6A, the band gap width of Fe_2O_3 is about 1.9 eV, and the positions of the conduction and valence bands correspond to 0.3 eV (Fig. S7A) and 2.2 eV, respectively. As shown in Fig. S6B, the band gap width of g-C_3N_4 is about 2.7 eV, and the positions of the conduction and valence bands correspond to − 1.05 eV (Fig. S7B) and 1.65 eV, respectively. Figs. S6C and S6D show the ultraviolet absorption curves of Fe_2O_3 and g-C_3N_4, with maximum absorption wavelengths of 652 nm and 455 nm, respectively. The Z-scheme heterojunction structure is formed due to the band gap structure matched by Fe_2O_3 and g-C_3N_4 [19]. When illuminated, the electrons and holes of Au NPs separate and migrate to the conduction and valence bands of Fe_2O_3, respectively. Then the electrons were excited from the valence band of Fe_2O_3 and g-C_3N_4 to the conduction band, respectively, and the holes were left in the valence band. The excited electrons migrate from the conduction band of Fe_2O_3 to the valence band of g-C_3N_4 and recombine the electron-hole pairs by d-p conjugation, thus inhibiting the compounding of the electron-hole pairs of Fe_2O_3. Immediately afterward, electrons are excited from the valence band of g-C_3N_4 to the conduction band. At the same time, electrons accumulate in the conduction band of g-C_3N_4, and holes accumulate in the valence band of Fe_2O_3 so that strong oxidation and strong reduction are maintained simultaneously. Finally, an anodic photocurrent is formed due to the flow of electrons to the working electrode (ITO), and the holes are neutralized by AA in the solution. When the Pb^{2+} is present, it competes with DNA-1 for DNA-2 to form G (Pb^{2+}-G4) chains dispersed in the solution when the spatial site resistance becomes small and the photocurrent signal is amplified. When the concentration of Pb^{2+} increases, the more G (Pb^{2+}-G4) chains are formed, the potential spatial resistance is further reduced, and the photocurrent is amplified sequentially. In this way, a PEC sensor capable of sensitively detecting the competitive signal amplification of Pb^{2+} was constructed.

3.5. Comparison of the electrode activity area

Evaluating the electrode surface active area is necessary because a large specific surface area will load more active sites. To compare the surface-active area of the substrate material and pure ITO, cyclic

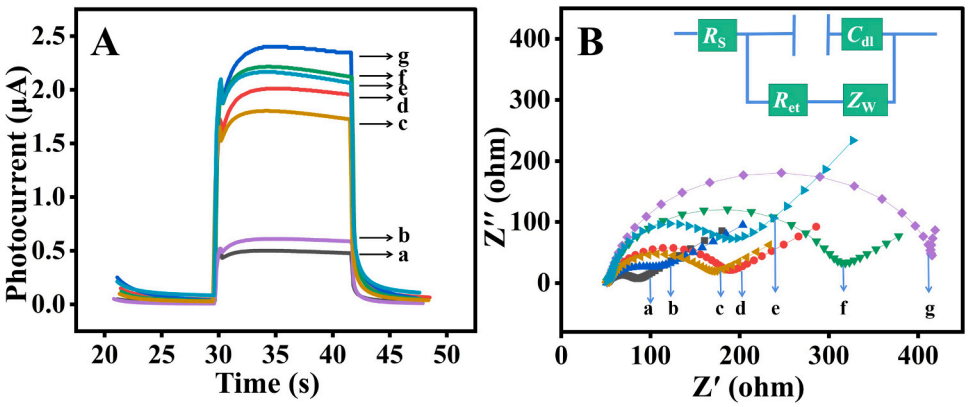

Fig. 4. (A) Photocurrent response (0.1 M pH 6.8 PBS containing 0.1 M AA), a: ITO/Fe_2O_3, b: ITO/Fe_2O_3/g-C_3N_4/Au/DNA-1/TGA/ZnO@DNA-2, c: ITO/Fe_2O_3/g-C_3N_4/Au/DNA-1/TGA/ZnO@DNA-2/Pb^{2+}, d: ITO/Fe_2O_3/g-C_3N_4, e: ITO/Fe_2O_3/g-C_3N_4/Au/DNA-1/TGA, f: ITO/Fe_2O_3/g-C_3N_4/Au/DNA-1, g: ITO/Fe_2O_3/g-C_3N_4/Au. (B) EIS curve (0.1 mol/L KCl containing 2.5 mmol/L $[Fe(CN)_6]^{4-/3-}$), a: ITO/Fe_2O_3, b: ITO/Fe_2O_3/g-C_3N_4, c: ITO/Fe_2O_3/g-C_3N_4/Au, d: ITO/Fe_2O_3/g-C_3N_4/Au/DNA-1, e: ITO/Fe_2O_3/g-C_3N_4/Au/DNA-1/TGA, f: ITO/Fe_2O_3/g-C_3N_4/Au/DNA-1/TGA/ZnO@DNA-2/Pb^{2+}, g: ITO/Fe_2O_3/g-C_3N_4/Au/DNA-1/ TGA/ZnO@DNA-2.

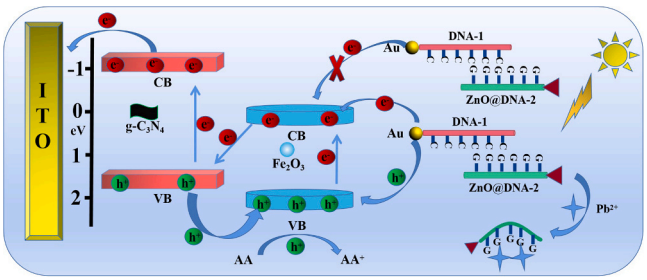

Fig. 5. Diagram of the electron transfer mechanism for PEC detection of Pb^{2+} in 0.1 M pH 6.8 PBS containing 0.1 M AA.

voltammetry (CV) tests were done on pure ITO and ITO/Fe_2O_3/g-C_3N_4. $[Fe(CN)_6]^{4-/3-}$ the solution was used as a redox probe. All analyses were based on the Randles Sevcik equation ($I = (2.69 \times 10^5)\, AD^{1/2}n^{3/2}v^{1/2}c$). Where I current peak varies with different scan rates, A is the electroactive surface area of the modified working electrode, and D is the value of the diffusion coefficient of $[Fe(CN)_6]^{4-/3-}$ of $(6.70 \pm 0.02) \times 10^{-6}$ cm^2/s, n is 1 indicating the number of electrons transferred in the redox reaction, c is the concentration value of $[Fe(CN)_6]^{4-/3-}$ of 5 mmol/L, and v is the scan rate of CV (V/s). The CV of pure ITO and ITO/Fe_2O_3/g-C_3N_4 were measured at different scan rates for Figs. S8A and S8C, respectively, and the regression equations for pure WE and ITO/Fe_2O_3/g-C_3N_4 were $I = 1470.1 \times v^{1/2} + 48.3$ ($R^2 = 0.976$) (Fig. S8B) and $I = 1805.7 \times v^{1/2} + 55.1$ ($R^2 = 0.992$) (Fig. S8D). The effective electrochemically active areas of pure ITO and ITO/Fe_2O_3/g-C_3N_4 were calculated to be 0.42 cm^2 and 0.51 cm^2, respectively. The results showed that the electrochemically active surface area of the modified ITO/Fe_2O_3/g-C_3N_4 nanocomposites increased by 21.4%.

3.6. Optimization of experimental conditions

To obtain the best PEC sensor performance, three important conditions were selected. The pH values of the solution, the concentrations of ascorbic acid (AA acts as an electron donor to neutralize the holes), and the concentrations of Fe_2O_3/g-C_3N_4 were optimized. The substrate material concentration affects the photocurrent magnitude to some extent. When the concentration is low, the substrate material affects the absorption of light energy and provides fewer electron transport sites. When the concentration is high, the substrate material hinders the transfer of photoelectrons. The pH of the solution is too low or too high can affect the activity of the aptamer, and neutral condition is a relatively appropriate environment. The presence of the electron donor ascorbic acid is one of the most important conditions to ensure that the photocurrent can be measured. Likewise, the concentration of AA is too low to provide enough electrons to neutralize the holes in the solution. At the same time, too much AA affects the electron-hole transfer rate. To verify whether there is a significant interaction between the three conditions, a Box-Behnken experiment was performed on three parameters. The concentration of substrate material ranges from 3 mg/mL to 7 mg/mL,pH ranges from 6.0 to 8.0, and the concentration of AA ranges from 0.08 M to 0.12 M. The experiment results are shown in Fig. 6A, B, and C. The resulting coding equation is as follows, $I = 1.950 - 0.0175A - 0.0325B - 0.015C - 0.0025AB + 0.025AC - 0.0225BC - 0.1162A^2 - 0.0962B^2 - 0.1063C^2$. When the substrate material is 4.9 mg/mL, pH is 6.8, and the AA concentration is 0.1 M, the photocurrent ($I = 1.954$ μA) response is the largest. When contours tend to be round, it means that there is no obvious interaction between the two. Otherwise, there is a clear interaction between the two. The contour contours in the figure do not tend to be elliptic, meaning that there is no significant interaction between the three parameters. In conclusion, we finally get the best experimental conditions: pH 6.8, the concentration of substrate material 4.9 mg/mL, and the concentration of AA 0.1 M.

3.7. Performance testing of sensor

An anodic PEC sensor was constructed with Z-scheme Fe_2O_3/g-C_3N_4 nanocomposite as the sensing platform, nucleic acid aptamer as the recognition unit, and ZnO@DNA-2 as the label for sensitive detection of Pb^{2+}. The relationship between the standard sample concentration of Pb^{2+} and the photocurrent was investigated. Fig. 7 A shows the trend of photocurrent versus lead ion concentration, which shows a good trend with increasing lead ion concentration. As shown in Fig. 7B, the photocurrent increased with increasing Pb^{2+} concentration from 62 pg/mL to 1 μg/mL under optimal conditions, showing a good linear relationship. The linear fitting equation was $I = (0.196 \pm 0.0098)$ lg $c + 0.82 \pm 0.041$ ($R^2 = 0.997$, 95% confidence interval, where I (μA) is the photocurrent, c (pg/mL) is the Pb^{2+} concentration), and the minimum detection limit was 7.9 pg/mL (S/N = 3). Since the constructed sensor has a wide detection range (62 pg/mL — 1 μg/mL) and a low detection limit (7.9 pg/mL), it performs well. As shown in Table S2, we compared other detection methods, and the present work has a good linear range, low detection limits, and good repeatability.

Stability is also an important element in evaluating the performance of the sensor. As shown in Fig. 7 C, the photocurrent response was tested for 14 consecutive switching light cycles under optimal test conditions, and the photocurrent values were kept in a flat state. Measured current values were 1.985, 1.980, 1.976, 1.973, 1.969, 1.966, 1.961, 1.958, 1.957, 1.956, 1.955, 1.951, 1.947, and 1.945 μA with RSD of 0.63%. It shows that the sensor has good test stability. The storage stability of the sensor was also tested, as shown in Fig. 7D, and the photocurrent maintained 98.2%, 95.5%, and 94.1% of the initial value under four consecutive weeks of testing. This proves the good storage stability of the designed sensor.

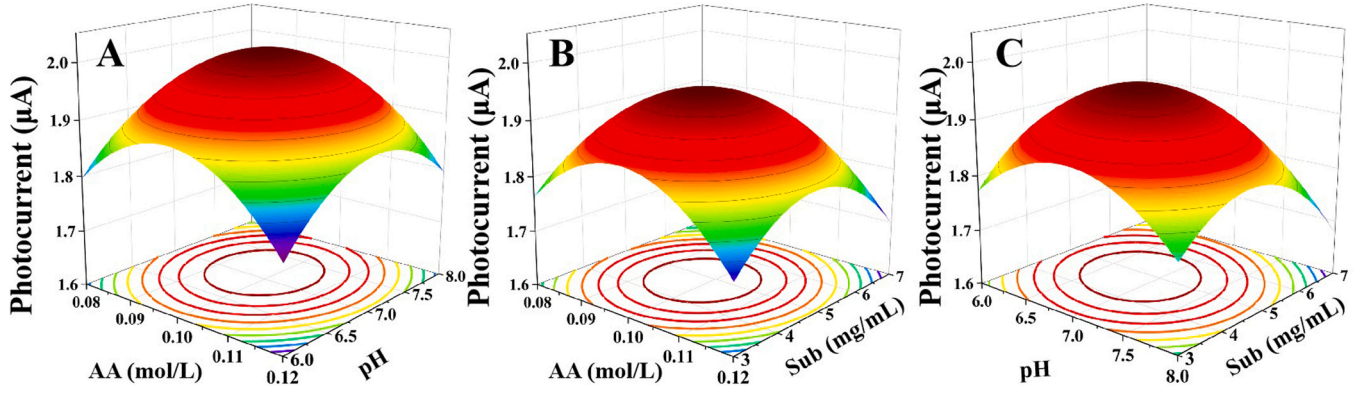

Fig. 6. Box-Behnken experiments of AA concentration, pH, and substrate (Fe_2O_3/g-C_3N_4) concentration (0.1 M PBS). (A—C) are 3D images of two factors interacting with each other, and the bottom of the figure are contour maps of the interaction of the two factors.

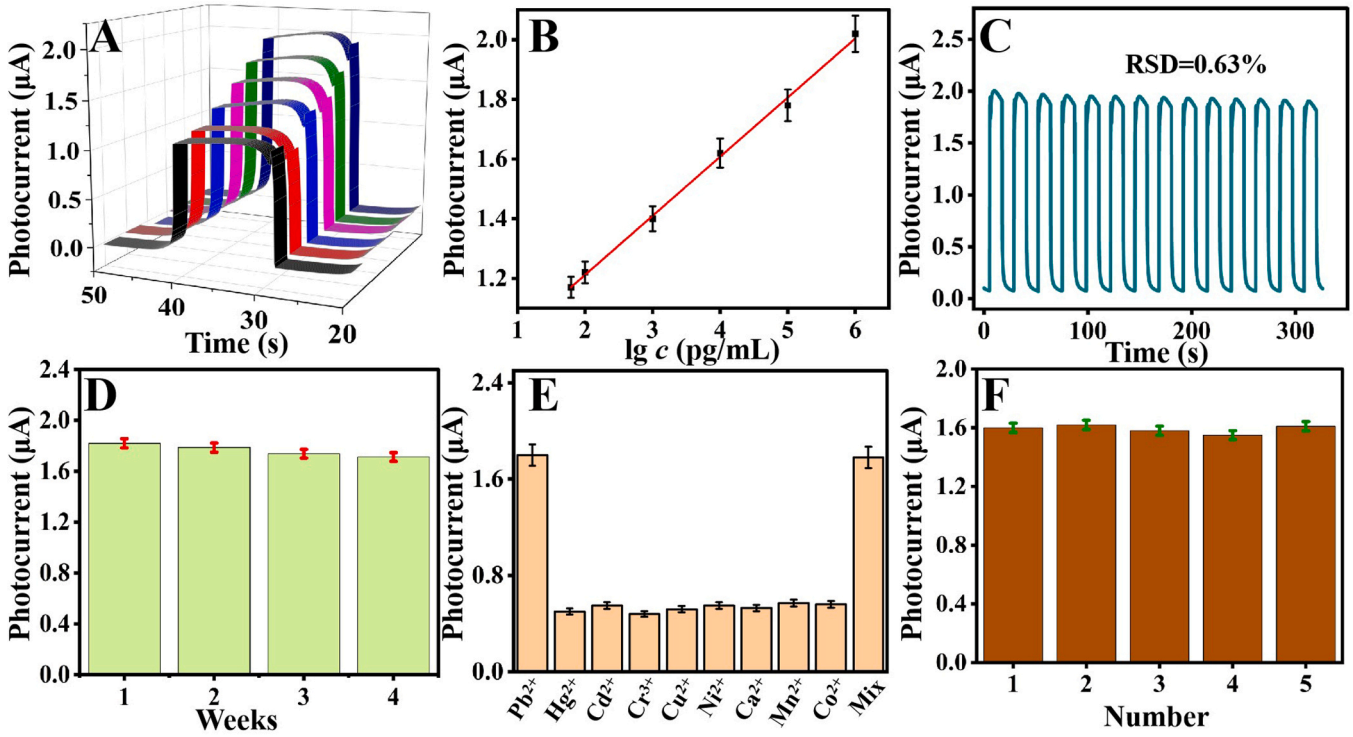

Fig. 7. (A) Photocurrent responses of the PEC sensors to 62, 10^2, 10^3, 10^4, 10^5 and 10^6 pg/mL Pb^{2+}, (B) logarithmic calibration plot of the sensor for different concentrations of Pb^{2+} with the equation, (C) stability of the sensor (1 μg/mL Pb^{2+}), (D) storage stability of PEC sensor (100 ng/mL Pb^{2+}), (E) photocurrent responses to 100 ng/mL Pb^{2+}, Hg^{2+}, Cd^{2+}, Cr^{3+}, Cu^{2+}, Ni^{2+}, Ca^{2+}, Mn^{2+}, Co^{2+}, and their mixture, (F) reproducibility of PEC sensor (100 ng/mL Pb^{2+}).

Selectivity is an important indicator to evaluate the sensor with good and excellent performance because non-specific binding can affect the accuracy of the detection results. Several common heavy metal ions were selected as references to verify the selectivity. As shown in Fig. 7E, Pb^{2+}, Hg^{2+}, Cd^{2+}, Cr^{3+}, Cu^{2+}, Ni^{2+}, Ca^{2+}, Mn^{2+}, and Co^{2+} were selected to compare the photocurrent response, and the sensitivity of the other ions to the sensor was negligible. Demonstrate that the designed sensor is specific for Pb^{2+}.

To evaluate the reproducibility of the sensor, five different experimental operators prepared one electrode each in the same environment. The measured current values were 1.60, 1.62, 1.58, 1.55, and 1.61 μA, respectively, with an RSD of 1.74% (Fig. 7 F). The specific good reproducibility of the sensor under different experimental conditions was demonstrated. Repeatability is an important index to test the accuracy of PEC sensor detection, and the RSD method was used to test the repeatability of the PEC sensor. Under the same environment, ITO electrodes with the same concentration were prepared at the same time. As shown in Fig. S9, five simultaneously modified 10 ng/mL Pb^{2+} were taken, and their photocurrent responses (1.61, 1.65, 1.57, 1.59, and 1.63 μA) were examined. The results showed that the RSD of the five samples was 1.96%, indicating that the PEC sensor has excellent repeatability.

3.8. Sample analysis

To investigate the performance of the constructed PEC sensor in real samples, the feasibility and accuracy of the sensor in real sample analysis were studied using the standard addition method. Taking the Jiazi Lake water and laboratory tap water of the University of Jinan as the detection object, 10 mL of sample was taken for activated carbon decolorization, centrifugation, and filtration was taken from the supernatant for use. The results are shown in Table 1. The average spiked recovery of the PEC sensor was 97%—110%, and the relative standard deviation was 1.24%—4.24%. Normal human serum was selected for the assay, and its recovery was 93%—102.2% with an RSD of 1.35%—3.45%. At the same time, we analyzed the samples for lead ion concentration by atomic absorption spectroscopy (AAS). As shown in Table S3, the experimental results were comparable to the PEC method. This indicates that this PEC sensor has great potential for application in real sample analysis.

Table 1
Analysis and recovery of samples from PEC sensor.

Sample	Added (ng/mL)	PEC found (ng/mL)	Recovery ($n = 5$, %)	RSD ($n = 5$, %)
Lake water	0	0.56		2.36
	0.10	0.67	110	1.56
	1.00	1.53	97	2.11
	5.00	5.59	100.6	4.24
Tap water	0	0.32		1.96
	0.10	0.41	90	1.24
	1.00	1.33	101	2.35
	5.00	5.34	100.4	3.54
Serum	0	15.22		2.64
	1.00	16.15	93	1.35
	5.00	20.25	100.6	2.64
	10.0	25.44	102.2	3.45

4. Conclusion

This work successfully constructed a novel PEC aptamer sensor for efficient and sensitive detection of Pb^{2+}. The Z-Scheme Fe_2O_3/g-C_3N_4 nanocomposite was used as the sensing platform, and the Z-scheme heterojunction provided strong charge transfer capability and maintained both strong oxidation and reduction properties. The gold nanoparticles serve as a bridge between the substrate material and DNA-1. The ZnO-labelled DNA-2 achieves signal amplification to construct a competitive PEC aptamer sensor capable of sensitive detection of Pb^{2+} in a wide detection range (62 pg/mL to 1 μg/mL). In addition, the Pb^{2+} sensor has good test stability, storage stability, specificity, and reproducibility. More importantly, the preparation process of sensing material has the advantages of being simple, low cost, and having no pollution. The sensor is expected to play a certain potential in the analysis of detecting heavy metal ions.

Environmental implication

Lead is a naturally occurring toxic metal in the earth's crust. Its widespread use has caused environmental contamination, human exposure, and major public health problems in many parts of the world. The prerequisite for lead ions removal is sensitive detection. Photoelectrochemical detection is of great importance due to the simplicity of the equipment, speed and high sensitivity. In this work, we have developed a photoelectrochemical aptamer sensor with Z-scheme Fe2O3/g-C3N4 heterojunction as a substrate material for sensitive detection of Pb2+.

CRediT authorship contribution statement

Jingui Chen: Writing – original draft, Data curation, **Jinxiu Zhao**: Data curation, Methodology. **Rui Feng:** Investigation, Experimental guidance. **Hongmin Ma**: Methodology. **Huan Wang**: Writing – review & editing. **Xiang Ren**: Data curation, Funding acquisition. **Qin Wei**: Funding acquisition, Experimental support. **Huangxian Ju**: Supervision, Formal analysis.

Declaration of Competing Interest

The authors declare that they have no known competing financial interests or personal relationships that could have appeared to influence the work reported in this paper.

Data Availability

No data was used for the research described in the article.

Acknowledgments

This study was supported by the National Natural Science Foundation of China (No.22204059, 22274062, 22206056), the Foundation of Yunnan Key Laboratory of Rural Energy Engineering (Yunnan Normal University), the Special Foundation for Taishan Scholar Professorship of Shandong Province (Prof. H.X. Ju and Prof. Q. Wei).

Appendix A. Supporting information

Supplementary data associated with this article can be found in the online version at doi:10.1016/j.jhazmat.2023.132122.

References

[1] Mahar, F.K., He, L., Wei, K., Mehdi, M., Zhu, M., Gu, J., et al., 2019. Rapid adsorption of lead ions using porous carbon nanofibers. Chemosphere 225, 360–367. https://doi.org/10.1016/j.chemosphere.2019.02.131.

[2] Sun, W., Ye, J., Lin, H., Yu, Q., Wang, Q., Chen, Z., et al., 2023. Dynamic characteristics of heavy metal accumulation in agricultural soils after continuous organic fertilizer application: Field-scale monitoring. Chemosphere 335, 139051. https://doi.org/10.1016/j.chemosphere.2023.139051.

[3] Feng, J., Chu, C., Dang, K., Yao, T., Ma, Z., Han, H., 2021. Responsive-released strategy based on lead ions-dependent DNAzyme functionalized UIO-66-NH_2 for tumor marker. Anal Chim Acta 1187, 339170. https://doi.org/10.1016/j.aca.2021.339170.

[4] Chris, D.I., Onyena, A.P., Sam, K., 2023. Evaluation of human health and ecological risk of heavy metals in water, sediment and shellfishes in typical artisanal oil mining areas of Nigeria. Environ Sci Pollut Res Int. https://doi.org/10.1007/s11356-023-27932-z.

[5] Liang, G., Man, Y., Li, A., Jin, X., Liu, X., Pan, L., 2017. DNAzyme-based biosensor for detection of lead ion: a review. Microchem J 131, 145–153. https://doi.org/10.1016/j.microc.2016.12.010.

[6] Ding, J., Liu, Y., Zhang, D., Yu, M., Zhan, X., Zhang, D., et al., 2018. An electrochemical aptasensor based on gold@polypyrrole composites for detection of lead ions. Mikrochim Acta 185, 545. https://doi.org/10.1007/s00604-018-3068-z.

[7] Zheng, Y., Li, Q., Wang, C., Su, M., 2021. Enhanced turn-on fluorescence detection of aqueous lead ions with size-shrinkable hydrogels. ACS Omega 6, 11897–11901. https://doi.org/10.1021/acsomega.1c00150.

[8] Dai, Y., Liu, C.C., 2017. A simple, cost-effective sensor for detecting lead ions in water using under-potential deposited bismuth sub-layer with differential pulse voltammetry (DPV). Sensors 17. https://doi.org/10.3390/s17050950.

[9] Zhou, Y., Yin, H., Ai, S., 2021. Applications of two-dimensional layered nanomaterials in photoelectrochemical sensors: a comprehensive review. Coord Chem Rev 447. https://doi.org/10.1016/j.ccr.2021.214156.

[10] Shu, J., Tang, D., 2020. Recent advances in photoelectrochemical sensing: from engineered photoactive materials to sensing devices and detection modes. Anal Chem 92, 363–377. https://doi.org/10.1021/acs.analchem.9b04199.

[11] Zhou, Y., Yin, H., Zhao, W.-W., Ai, S., 2020. Electrochemical, electrochemiluminescent and photoelectrochemical bioanalysis of epigenetic modifiers: a comprehensive review. Coord Chem Rev 424. https://doi.org/10.1016/j.ccr.2020.213519.

[12] Zhang, J., Xue, X., Du, Y., Zhao, J., Ma, H., Ren, X., et al., 2022. Antigen-down PEC immunosensor for CYFRA21-1 detection based on photocurrent polarity switching strategy. Anal Chem 94, 12368–12373. https://doi.org/10.1021/acs.analchem.2c01478.

[13] Chen, J., Zhao, J., Feng, J., Wu, D., Ma, H., Ren, X., et al., 2022. Photoelectrochemical immunosensor based on a 1D Fe_2O_3/3D Cd-$ZnIn_{2.2}S_y$ heterostructure as a sensing platform for ultrasensitive detection of neuron-specific enolase. Anal Chem 94, 17396–17404. https://doi.org/10.1021/acs.analchem.2c02645.

[14] Dong, X., Zhao, G., Li, Y., Zeng, Q., Ma, H., Wu, D., et al., 2022. Dual-mechanism quenching of electrochemiluminescence immunosensor based on a novel ECL emitter polyoxomolybdate-zirconia for 17 beta-estradiol detection. Anal Chem 94, 12742–12749. https://doi.org/10.1021/acs.analchem.2c02350.

[15] Govindaraju, G.V., Wheeler, G.P., Lee, D., Choi, K.-S., 2016. Methods for electrochemical synthesis and photoelectrochemical characterization for photoelectrodes. Chem Mater 29, 355–370. https://doi.org/10.1021/acs.chemmater.6b03469.

[16] Li, F., Zhou, Y., Yin, H., Ai, S., 2020. Recent advances on signal amplification strategies in photoelectrochemical sensing of microRNAs. Biosens Bioelectron 166, 112476. https://doi.org/10.1016/j.bios.2020.112476.

[17] Ho-Kimura, S., Luo, W., 2021. Reinforcement of a $BiVO_4$ anode with an Fe_2O_3 underlayer for photoelectrochemical water splitting, Sustainable. Energy Fuels 5, 3102–3114. https://doi.org/10.1039/d1se00310k.

[18] Xu, W., Xue, W., Huang, H., Wang, J., Zhong, C., Mei, D., 2021. Morphology controlled synthesis of α-Fe_2O_3-x with benzimidazole-modified Fe-MOFs for enhanced photo-Fenton-like catalysis. Appl Catal B: Environ 291. https://doi.org/10.1016/j.apcatb.2021.120129.

[19] Li, L., She, X., Yi, J., Pan, L., Xia, K., Wei, W., et al., 2019. Integrating CoO_x cocatalyst on hexagonal α-Fe_2O_3 for effective photocatalytic oxygen evolution. Appl Surf Sci 469, 933–940. https://doi.org/10.1016/j.apsusc.2018.11.014.

[20] Jiang, Y., Ding, Q., Yuan, R., Liu, G., Yuan, Y., 2023. Photoactive conjugated microporous polymer@C_{60} with quencher on tailed Y-triangular DNA structure for high-performance signal-off photoelectrochemical biosensing. J Hazard Mater 457, 131724. https://doi.org/10.1016/j.jhazmat.2023.131724.

[21] Liu, C., Meng, F., Zhang, L., Zhang, D., Wei, S., Qi, K., et al., 2019. CuO/ZnO heterojunction nanoarrays for enhanced photoelectrochemical water oxidation. Appl Surf Sci 469, 276–282. https://doi.org/10.1016/j.apsusc.2018.11.054.

[22] Xu, Q., Zhu, B., Jiang, C., Cheng, B., Yu, J., 2018. Constructing 2D/2D Fe_2O_3/g-C_3N_4 direct Z-scheme photocatalysts with enhanced h2 generation performance. Sol RRL 2. https://doi.org/10.1002/solr.201800006.

[23] Wang, S., Zhao, T., Tian, Y., Yan, L., Su, Z., 2021. Mechanistic insight into photocatalytic CO_2 reduction by a Z-scheme g-C_3N_4/TiO_2 heterostructure. N J Chem 45, 11474–11480. https://doi.org/10.1039/d0nj05681b.

[24] Inkpen, M.S., Liu, Z.F., Li, H., Campos, L.M., Neaton, J.B., Venkataraman, L., 2019. Non-chemisorbed gold-sulfur binding prevails in self-assembled monolayers. Nat Chem 11, 351–358. https://doi.org/10.1038/s41557-019-0216-y.

[25] Sui, C., Li, F., Wu, H., Yin, H., Zhang, S., Waterhouse, G.I.N., et al., 2019. Photoelectrochemical biosensor for 5hmC detection based on the photocurrent inhibition effect of ZnO on MoS_2/C_3N_4 heterojunction. Biosens Bioelectron 142, 111516. https://doi.org/10.1016/j.bios.2019.111516.